STUDY OF MECHANICAL PROPERTIES OF AZ91 MAGNESIUM ALLOY WELDED BY LASER PROCESS TAKING INTO ACCOUNT THE ANISOTROPY MICRO-HARDNESS AND RESIDUAL STRESSES BY X-RAY DIFFRACTION

[1✉]A. Kouadri, [2]L. Barrallier

[1✉]PSM Team (Correspondant author), European university of Brittany, France, INSA, LGCGM, EA 3913, 20 Avenue des Buttes des Coesmes, F-35708 RENNES, [2]MecaSurf Team, Arts et Métiers Paris Tech, France, ENSAM, Mecasurf, JE2504, 2 cours des arts, 13617 Aix en Provence, (France)

ABSTRACT

The objective was to study the mechanical properties of a magnesium alloy welded by a CO_2 laser. Residual stresses were measured by X-ray diffraction. They were calculated by the classic $\sin^2\Psi$ method in the isotropic zones by using the orientation distribution function (ODF) in the textured zones. The results demonstrated that laser welding results in the formation of a number of different zones with different microstructural and mechanical properties. Welding principally leads to a reduction in grain size and a new distribution of phases. The most remarkable observation was that of a superficial layer on the surface of the welded zone. This layer has the peculiarity of a marked crystallographic texture, a reduction in the level of aluminium as well as an elevated microhardness. These characteristics disappear after a depth of 200μm under the welded zone. These modifications can be explained by the nature of the solidification which occurs under nonequilibrium conditions resulting in an equiaxial columnar transition. This transition is also evident within the profile of residual tensile stresses which are at their maximum at the interface between the superficial layer and the rest of the welded zone. These results are explained by the anisotropic properties of the textured layer in relation to the plasticity.

1. Introduction

There is a large potential for weight savings by using magnesium alloys. Their use for structural parts is growing and allows manufacturers to reduce the weight of such parts in industries such as automotive, computing, communications and electronics. The demand for lighter and thinner products has led to magnesium alloys being machined under various conditions, especially with fast cooling like laser welding. The performance of the material under thermal, mechanical and other kinds of loading depends on the state of residual stresses induced during the manufacturing process. Residual stresses play an important part in the performance of operating mechanical parts. Their effects on the different properties of materials (fatigue, rupture, corrosion, friction, etc.) can be considerable [1]. Following the employed process, several studies have shown that these stresses heavily induce brittle fracture and degrade the buckling strength of built structures [2]. Welding, which is employed more and more, is one of the most important technological processes used in many branches of industry such as industrial engineering, shipbuilding, and pipeline fabrication among others. In this study, laser welding has been used to weld new light alloys such as magnesium. In particular, this technique is a complex process accompanied by shrinkage effects, phase transformations and intensification of corrosion [3]. This process leads to solidification in nonequilibrium conditions. It has been reported that rapidly solidified Mg alloys exhibit a change of the microstructure and especially a grain refinement [4], a formation or a modification of the texture [5] and the presence of residual stresses [6].

The base material properties are superior but the weakest link in the application of these alloys is the properties of the weldments. During welding, a substantial residual stress field may develop, as it necessarily involves large temperature gradients from weld metal to bulk material. Residual stresses may reach and even exceed the plastic yield point of the base metal being welded with both tensile and compressive residual stresses in different zones of the welded structure. However a number of questions remain on the effect of this type of welding on the mechanical aspects of these assembled structures. In this case, it is essential to have precise knowledge of the variation of residual stress across the weld and near the weldment. This problem is at the heart of this study.

The objective of this study is to characterize the mechanical properties with the calculus of the residual stresses and of the microhardness in every zone of the welded sheet. This work characterized the microstructure modification (characterization of the grain size, chemical properties and the crystallographic texture) occurring during laser welding on these properties. The studied material is a magnesium alloy (AZ91) welded by laser processing. The residual stresses have been performed by taking into account the crystallographic texture. The strain measurements and the characterization of the crystallographic texture have been performed using X-ray diffraction techniques.

2. Stress calculus methodology

2.1 Principle of diffraction and use of the Bragg law

Residual stress measurements were performed using X-ray diffraction. X-ray residual stress analysis was based on the angular shift of diffraction lines due to stresses. This technique uses the distances between atomic planes as an internal strain gauge. Bragg's law (Eq.1) gives the relation between the spacing d of lattice planes of the crystallites of a polycrystalline material and the angular position θ of diffraction lines using monochromatic X-rays of wavelength λ.

$$2d_{\phi\psi} \cdot \sin\theta_{\phi\psi} \;=\; n.\lambda \qquad \textbf{Eq.1}$$

Thus, lattice strains can be evaluated from angular shifts of the diffraction lines:

$$\varepsilon_{\phi\psi} \;=\; \frac{d_{\phi\psi} - d_0}{d_0} \;=\; -(\theta_{\phi\psi} - \theta_0)\cot\theta_0 \qquad \textbf{Eq.2}$$

In order to increase the reliability of measurements and to make the measurements less sensitive to the exact d_0-value, the strain distribution was determined with several angles ϕ within the sample surface area and at different tilt angles Ψ within an area perpendicular to the sample surface (see figure 1). Thus, measurements of peak shifts were performed for various azimuth angle ϕ, and Ψ tilt angles.
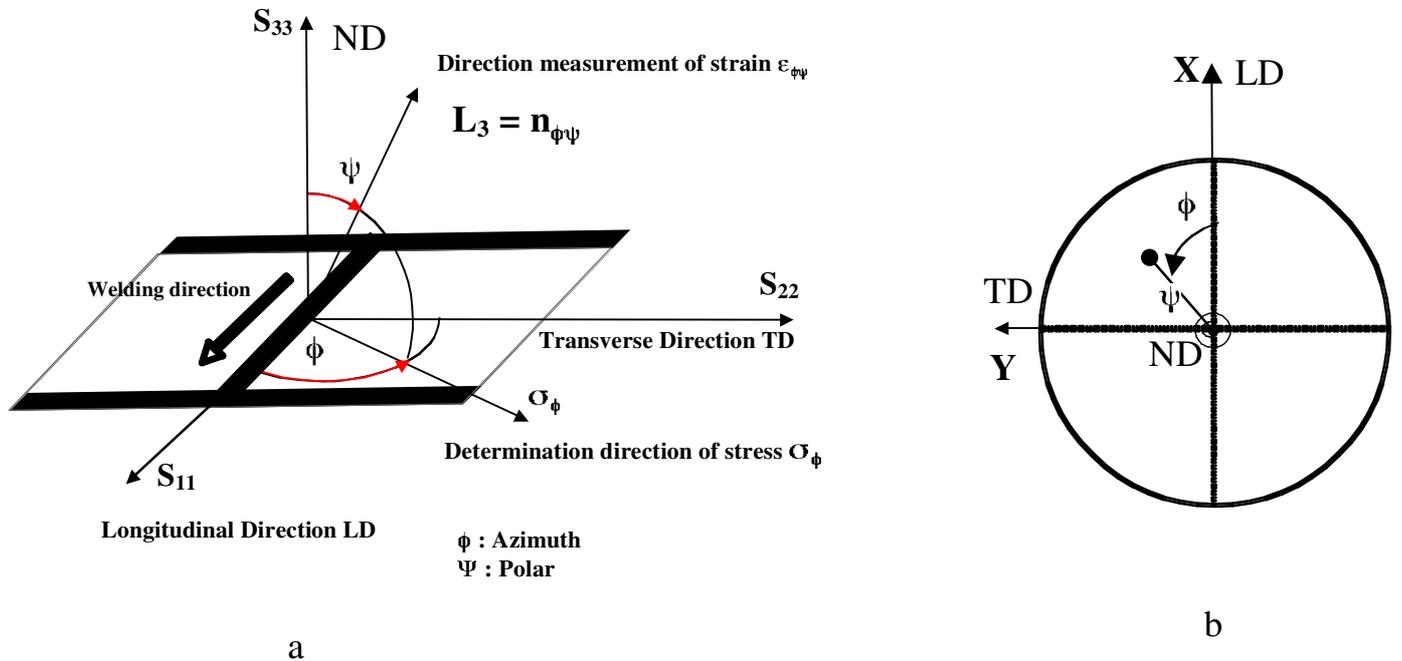
Figure 1: (a) Orientation of strain components $\varepsilon_{\phi\Psi}$ and of the stress components σ_{ϕ} with respect to the coordinate system S_{11}, S_{22}, S_{33} of the sample and (b) those of the sample for the areas measured.

In our study, the measurements were performed close to the surface of the sample due to the low penetration of the X-ray. To estimate the average residual stresses in every location, we made the hypothesis that there exists a planar system of the stresses σ_1 and σ_2 ($\sigma_3 = 0$).

2.2 Calculus of residual stresses and choice of parameters

The calculus of residual stresses required a number of steps:

2.2.1 Identification of crystalline phases

The identification of crystalline phases was undertaken by indexing diffraction peaks. The position of the diffraction peaks was defined by the optimisation of the parameters by a "pseudo – Voigt" ($K_{\alpha 1}$ et $K_{\alpha 2}$) function of the intensities of diffraction. The information collected allowed for determining which family of crystal planes will be used as an internal gauge and consequently the settings to adopt for measuring the deformations $\varepsilon_{\varphi\psi}$.

Two phases were present: α-Mg and β-$Mg_{17}Al_{12}$. The following study was undertaken without using the contribution of the β phase. There were a number of reasons for this choice. The elastic constants of the β-$Mg_{17}Al_{12}$ phase necessary to calculate the residual stresses were unknown: this phase does not exist alone. We also did not have a model, which taked into account the $\varepsilon_{\varphi\psi}$ deformations of the two phases. Furthermore the realized thermodynamic calculations using "Thermocalc" software show that this phase represented less than 15% of the base material and 10 % in the welded zone.

2.2.2 ODF calculation

The analysis of the texture was only done for the majority phase: the α-Mg matrix. The textures were obtained by choosing 5 pole figures, which corresponded respectively to the diffraction planes of the main α-Mg phase: the prismatic plane $\{10\bar{1}0\}$, basal plane $\{0002\}$,

pyramidal plane $\{10\bar{1}1\}$, pyramidal of the first order plane $\{10\bar{1}2\}$ and prismatic plane $\{11\bar{2}0\}$. The intensities diffracted, expressed by the number of strikes per second, are recorded by the variation of two angles: the polar angle ψ, variation from 0 to 70° from the axial direction of the sample by 5° steps, and the azimuthal angle φ, variation from 0 to 360° by 10° steps from the reference angle of the plane of the sample. Corresponding time was 4 hours per pole figure.

Poles figures were plotted using a standard stereographic projection with the welding axis (Z) and the longitudinal reference direction at the North Pole as shown (figure 1.b). The selected reference system was with the Z-axis normal to the plates (ND: normal direction). The X and Y directions were on the plane parallel to the metal and correspond respectively to the longitudinal direction (LD) and to the transverse direction (TD).

The orientation distribution function (ODF) was calculated from five complete pole figures, using a discrete method ADC (Arbitrarily Defined Cells method) [7, 8, 9]. The complete pole figures were calculated using "Labotex" software. The volume fraction of each component, g, has been calculated by integration around each orientation in the ranges given by chosen set of texture components and for each Euler angle [10]. The chosen orientations have been entered with the following values of the Euler angles: $\Phi_1 = 65.6°$, $\varphi = 60.8°$, $\Phi_2 = 54.4°$ for the   orientation and $\Phi_1 = 65°$, $\varphi = 90°$, $\Phi_2 = 60°$ for the orientation.

2.2.3 Measurement of deformations $\varepsilon_{\varphi\psi}$

The $\varepsilon_{\varphi\psi}$ deformations were deduced from the angular difference between the diffraction peaks. For the deformation measurements the diffraction plane of the magnesium phase was chosen. The measurements were done by simultaneous variation of 11 polar angles Ψ, with $\pm$ 65° variation, distributed in $\sin^2\Psi$, and 6 azimuth φ angles varying from 0 to 360°.

2.2.4 Residual stress calculations

2.2.4.1 Case of an isotropic material

When the material is macroscopically isotropic, the residual stresses are evaluated using the classical $sin^2\psi$ law, which assumes that a planar system exists for the stresses σ_1 and σ_2 ($\sigma_3 = 0$):

$$\varepsilon_{\phi\psi} = \frac{1}{2} S_2 \sigma_\phi . sin^2\psi + S_1(\sigma_{11}^S + \sigma_{22}^S) \qquad \textbf{Eq.3}$$

The strain distribution $\varepsilon_{\phi\psi}$ is plotted versus $sin^2\psi$ for a constant azimuth angle ϕ. Therefore X-ray elastic constants (S_1 and $1/2S_2$) were calculated from magnesium single-crystal compliances, assuming the material as macroscopically isotropic [11]. This was done using the Kröner-Eshelby model. The values used to calculate the residual stresses are as follows: S_1 (- 5.58×10^{-6} MPa^{-1}) and S_2 (26.04×10^{-6} MPa^{-1}).

2.2.4.2 Case of a textured material

In the case of a crystallographic texture inducing elastic anisotropy, the $sin^2\Psi$ method is no longer valid. There is no linearity of the distribution of $\varepsilon_{\phi\Psi}$ (hkl) vs. $sin^2\Psi$. Then, the calculations of the residual stresses must be evaluated taking into account the orientation distribution function (ODF). ODF and $\varepsilon_{\phi\Psi}$ data are used in conjunction with the Kröner-Eshelby model [12, 13], to calculate the residual stresses induced by the laser process. In this way all the orientations, through the ODF, contribute to the description of the mechanical behavior of the aggregate. The strains calculated from data acquired at the micrometer scale, $\varepsilon_{\phi\Psi}$(hkl), can be related to macrostresses by the following Eq.4:

$$\varepsilon_{\phi\psi}(hkl) = F_{ij}^{hkl}[s(\Omega), S, ODF(\Omega), \Phi, \Psi] \sigma_{ij}^I \qquad (i, j = 1 \text{ to } 3) \qquad \textbf{Eq.4}$$

Where:

a. The coefficients F_{ij} are called X-ray elasticity constants (XEC).

b. The Ψ angle is defined as the rotation about an axis lying along the intersection of the plane

of the substrate with the X-ray incidence plane. φ is the azimuth angle.

c. Ω represents the three Euler angles between the crystal coordinate system and the sample coordinate system.

d. s(Ω) represents the single crystal compliances in the sample coordinate system.

e. S is the macroscopic anisotropic compliance tensor of the material,

f. ODF is the orientation distribution function of the diffracting domains,

g. The superscript I represents for first order stresses.

The X-ray elastic constants are calculated numerically and are used in this method. The calculated strains are plotted as a function of F_{ij}. The slope of the curve then represents the stress in the sample. Equation (4) becomes:

$$\varepsilon_{\phi\psi}(hkl) = F_{11}(hkl, s, S, ODF, \Phi, \Psi)\ \sigma_{11} + F_{22}(hkl, s, S, ODF, \Phi, \Psi)\ \sigma_{22} + F_{12}(hkl, s, S, ODF, \Phi, \Psi)\ \sigma_{12}$$

Eq.5

Since measurement technique is the diffraction of X-rays, only the superficial layer of the metal (a few micrometers) interacts with the X-ray beam. The stress state was considered as planar ($\sigma_3 = 0$).

3. Experimental methods

3.1 Sample presentation

The alloy used for the study of the laser welding is a ternary magnesium - aluminum - zinc alloy with the designation AZ91, according ASTM standard. The sheets of AZ91 alloy, presented in figure 2, come from an industrial source (Messnier Foundries).
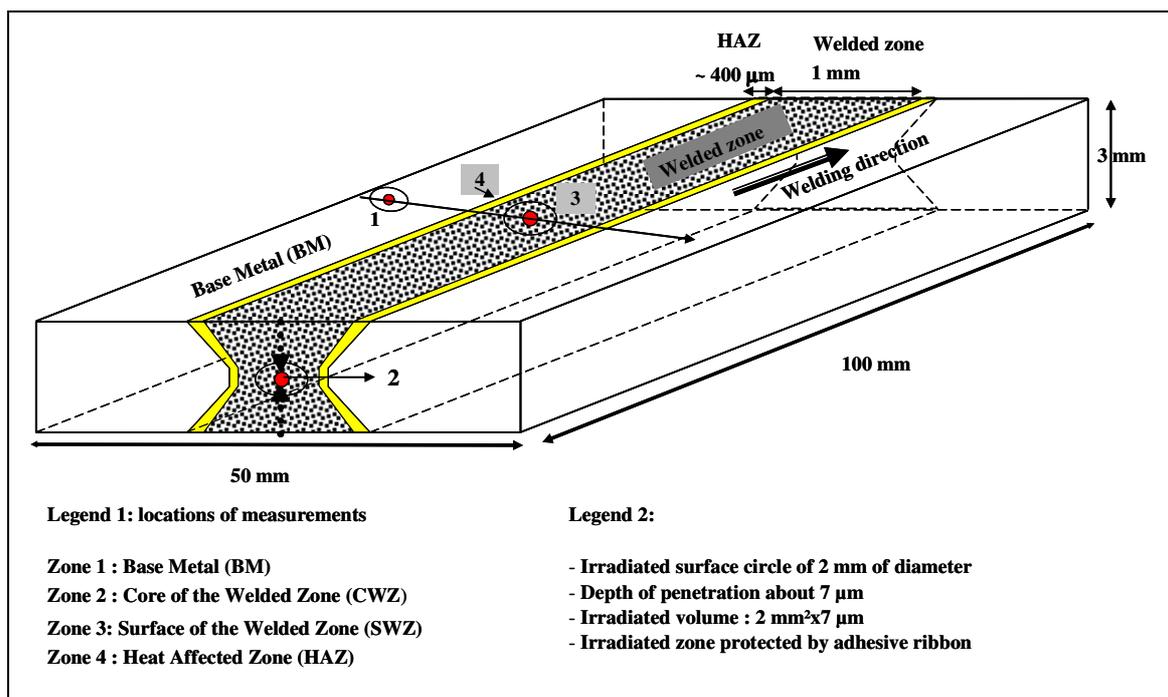
Figure 2: Geometric dimensions of the material and locations of the measurements

They were obtained by high pressure die casting under neutral gas and did not undergo heat treatment to be the as-cast condition, generally used in the automobile applications. The provided plates were sheared to recover the 3 mm thickness parts. Their edges were machined by milling. For the experimental study performed within the framework of our work, we had machined samples with parallelepidic shape and dimensions of 300x46x3 mm^3. Two plates were welded together side by side using a laser beam, which penetrated throughout the thickness of the plates. The welding used a 4000 W CO_2 laser in an inert helium atmosphere (2 bars). The speed of welding was optimized in the range of 1.0 – 4.25m/min.

3.1.1 Measurements locations

Figure 2 shows the sample. In the center of the plate, a welding zone crosses the whole length of the sample. Two series of measurements were undertaken. The first was undertaken on the surface from the base metal (BM: zone 1) towards the center of the welding zone (SWZ: zone 3) and passing through the zone of metal affected thermally (HAZ: zone 4), and perpendicular

9

to the weld line. The second series of measurements were undertaken in the weld line throughout its thickness (CWZ: zone 2), which necessitated progressive removal of material.

3.1.2 Measurements locations in the depth of the welded zone

Matter removal by chemical means was necessary in order to measure the stress tensor at an interior point of a solid by means of X-ray diffraction. This removal leads towards a relaxation and redistribution of residual stresses. This is why we performed an electrochemical polishing. A 5 mm diameter discs were electrochemically polished in a Struers Tenupol-3 jet polisher at a temperature below 10°C with a 14 V polishing voltage. The polishing solution was 10% HCl, 90% $C_4H_9OCH_2CH_2OH$ (butoxy-2-ethanol) by volume. Material removal was performed by applying a voltage and shooting a jet of an electrolyte at a side of the sample. Large areas of the sample were then thinned without introducing any mechanical damage. The process stopped automatically when a hole is made in the specimen. Checks of depths were performed using a comparator in order to confirm the depth of polishing, in our case 200 µm.

In this study, the polishing done by electrochemical means forms a slight bowl compared to the thickness of the sample. The size of the hole (diameter of 5 mm) represented less than 5% compared to the length of the sample, less than 10 % of the width of the sample and less than 10% compared to the thickness of the sample. Due to the large thickness of the sample (< 2 mm), correction for material removal was not necessary in the residual stresses studies. The obtained residual stresses were average values and we only discussed the average residual stresses.

The profile of the residual stresses through all the thickness was the joining together of two series of measurements, the first from the upper surface towards the center and the second from the bottom surface towards the center. The two polishing sites were offset and followed

the axis of the weld line. The distance between the measured points in the weld seam has been obtained by a weak shift of the irradiated zone using a comparative scale.

3.2 Observations of the microstructure

This part was already described in another publication [14]. The aim of this publication was to have a detailed description of the microstructural properties using scanning electron microscopy (SEM), crystallographic texture, X-ray diffraction analysis for the identification of the phases and evolution of the chemical properties in every studied zone. For a better correlation between the microstructure and the mechanical properties, we made a summary of these results. The observations we added in this work include the results obtained in optical microscopy and the average of the grain sizes obtained by image analysis.

3.2.1 Grain sizes measurement by microscopy optical

The aim of this part is to have a detailed description of the microstructural properties (distribution of the grains size) in every studied zone. The microsections for the structure examination were first polished with sandpaper of 450 to 1200 grits and then mechanically polished with 3 and 1 µm diamond oil-suspension. After polishing, the structure was revealed by 3%-nital solution, composed by 100 ml CH_3OH + 3 ml HNO_3. The microstructures in every zone were investigated by scanning electron microscopy (SEM) [14] and by optical microscopy.

3. 2 Image analysis procedure

The distribution of the grain size and the quantities of different fractions present in the base metal and in the melted zone were obtained by image analysis from several microstructures studied by optical microscopy (figure 3a and 3b). The analysis of the image was done using a camera combined with an optical microscope. The images were analysed using the ImageJ

software, which allows for surfaces to be defined and grains to be counted and grouped into diameter groupings. The distribution of the grain size was obtained via the method of grain counting per unit area (Np) in different 2-D sections obtained from the optical microscopy. Because the material had a heterogeneous distribution, we used the iterative method which uses the distribution of the diameters of the circles obtained [15]. We used different classes to distinguish the different phases present. By counting the number of grains we calculated the volume fractions of the phases by using the Fridy and al [16] ratio which states that the volume fraction is equal to the ratio of surface cuts: $V_v = A_a$.

3.3 Texture characterization and Strains measurement by X-ray diffraction

From the crystallographic and strains measurement point of view, the results were drawn from X-ray diffraction into obvious described locations: zones 1, 2 and 3. The diffractometer is equipped with a four-circle goniometer (Seifert MZ VI - TS). The X-ray source has a 1 mm point collimator and the goniometer is equipped with a position sensitive detector (PSD). Cr-Kα radiation was used to perform the phase and the texture analysis. Generator current and voltage levels used were 30 mA and 40 kV. The irradiated zone was limited by a 0.8 mm mask (Figure 2). Under these conditions the depth to which the alloy is penetrated is estimated at 7µm. The results were described in [14].

3.4 Hardness measurement

The microhardness was measured by a Vickers indenter under a load of 100 g on cross sections applied for 15 sec. A program on a conventional optical microscopy measured the diagonal lines of the mark. Two measurement series have been realized, one close to the surface from the SWZ until the BM in every location and the other with the same profile at a depth around 200 μm in every location. Microhardness samples were made from 3 mm thick plates. Samples were ground to an approximate thickness between 50 and 180 μm using grit

silicon carbide polishing papers with sandpaper of 450 to 1200 grit and then mechanically polished with 3 and 1 µm diamond oil-suspension. Afterwards, we followed the same procedure as that described for the residual stresses. Discs with 10 mm diameter were electrochemically polished in a Struers Tenupol-3 jet polisher at a temperature below 10°C with a 14 V polishing voltage. The polishing solution was 10% HCl, 90% $C_4H_9OCH_2CH_2OH$ (butoxy-2-ethanol) by volume. Large areas of the sample were then thinned without introducing any mechanical damage. The process stopped automatically when a hole was made in the specimen. Checks of depths were performed using a comparator in order to confirm the depth of polishing of 200 µm.

4. Experimental results of the microstructure

4.1. Summary of the microstructure and phase analysis

This part of the paper was taken from reference [14]. The base metal exhibits small precipitates dispersed in the matrix but mainly located at the grain boundaries. These precipitates are β-$Mg_{17}Al_{12}$ and to a lesser degree Al_8Mn_3. The matrix itself is heterogeneous. The mean grain sizes range from 50 to 200 µm (see figure 3a).

| a | Base metal | b | Welded zone | Heat Affected Zone |
| | 50-200 µm | | 10-25 µm | 50-200 µm |
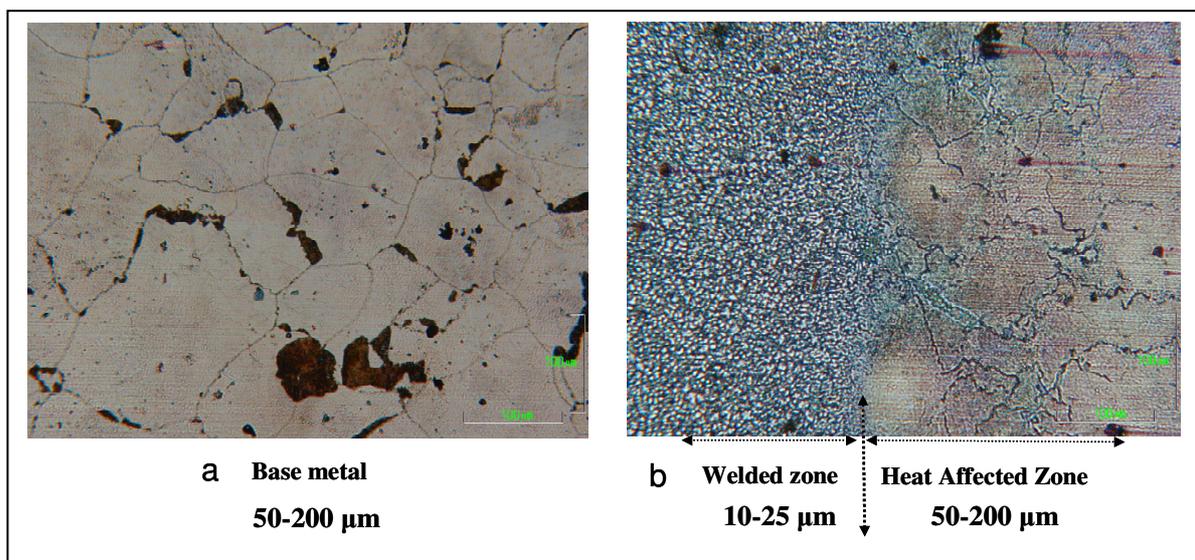
Figure 3: a) Microstructure of the base metal, solid solution α-Mg and (α-Mg + β-$Mg_{17}Al_{12}$) eutectic phase, b) in the welding zone and in the heat affected zone by (OM).

It is characterised by a mixture of a large primary α-Mg phase and of a (α-Mg + β-Mg$_{17}$Al$_{12}$) eutectic phases. This later constituent is a so-called abnormal eutectic [3, 14, 17] because of its lamellar shape. The predominance of the α-Mg phase is confirmed by X-ray analysis [14]. Peaks corresponding to β-Mg$_{17}$Al$_{12}$ appear clearly too, but to a lesser degree. Finally a third class of peaks is observed which corresponds to the superposition of the two phases, α and β (for example $2\theta = 117°$). In the welded zone, the microstructure is very different from the base metal. The α-Mg microstructure is much finer ranging between 10µm and 25µm. There is β-Mg$_{17}$Al$_{12}$ precipitates too, clearly present and located in grain boundaries [14]. So, the microstructure appears to be more homogenous at scale lengths of a few micrometers. The phase analysis [14] shows that there is no longer a (α + β) eutectic phase, or at least, that the volume fraction is very small. The height of the peaks corresponding to the β-phase [14] in the welded zone close to the surface does not change much even if their height decreases lightly. These results of the phase analysis can be explained by the presence of a texture, which can be responsible for this decrease. It is the reason for which no quantitative analysis should be performed without an analysis of the texture. The region with a width of about 200 – 500 μm between the base metal and the fusion zone can be recognized as the heat affected zone (HAZ). The typical overall microstructure of a HAZ is shown in figure 3b and in [14]. The microstructure of HAZ has coarse grain polygonal Mg as the base metal. Nevertheless, eutectic grains disappeared whereas a continuous β-Al$_{12}$Mg$_{17}$ phase was created at grain boundary.

4.2 Chemical analysis

The chemical composition (% weight.) of each individual phase in the different phases was studied using EDS analysis [14]. The base metal [14] will constitute a reference state for the comparison with the welded area. Energy dispersive spectroscopy (EDS) analysis indicated

that the α-Mg grain contains up to 8.1 and 1.15 wt.% of Al and Zn, respectively. The β-phase

contains ≈ 32 wt.% Al. All these results were in complete agreement with the literature on

AZ91 alloy microstructure, which has been widely studied [3, 4, 17].

In the HAZ, higher Al and Zn concentrations in the α-phase were measured as compared to

the base metal and to the welded zone [14]. So, this confirms that β-$Mg_{17}Al_{12}$ and Al_8Mn_3

precipitates were diluted in a matrix made of over-saturated α-phase.

In the welded zone, the chemical composition of phases was much the same as in base metal

[14] except in a thin superficial layer. The Al-content in the α-phase decreases from 30 %

(weight) in the BM and the CWZ down to 17% (weight) in the SWZ. Likewise, we could see

a strong decrease of the Al-content in every crystalline phase [14]. We concluded that there

was a loss of the overall Al quantity, due to the solidification conditions [3, 14, 18].

4.3 Distribution of grain size and volumetric fractions of phases by image analysis

The statistical distribution of the different grain sizes obtained by grain count is presented in

figure 4a.

a   b
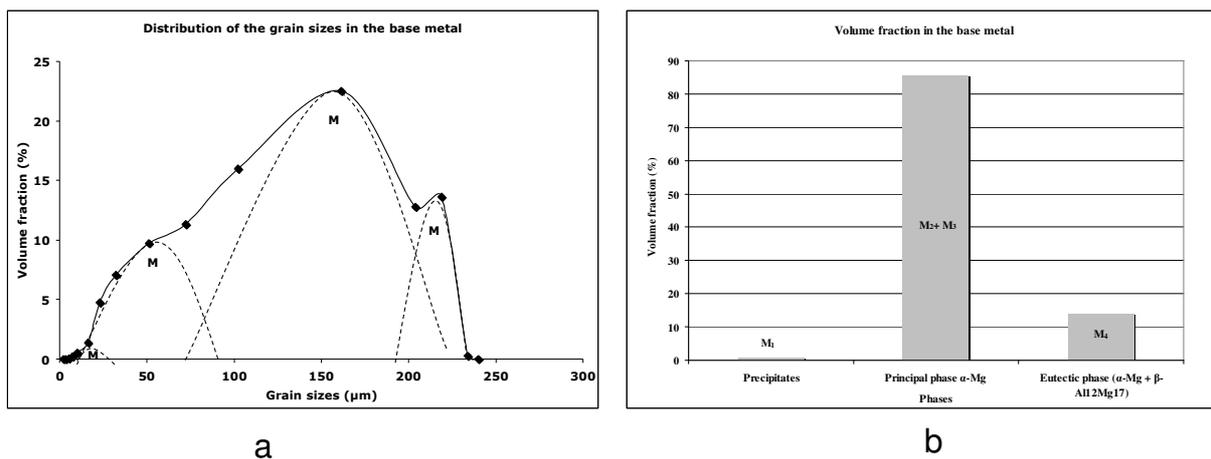
Figure 4 : (a) Statistical distribution of the grain sizes of AZ91 alloys in the base metal. (b)

Volume fraction of the α-Mg grains, of the eutectic (α-Mg grains β-$Mg_{17}Al_{12}$) phase and of

the precipitates in the base metal.

This distribution shows the presence of four modes; M_1, M_2, M_3 and M_4: The precipitates (M_1), whose main mode is about 10 µm and the principal α-Mg ($M_2 + M_3$) phase, whose main modes are 50 and 160 µm. Finally the principal mode of the eutectic phase (α-Mg + β-$Al_{12}Mg_{17}$) is about 220µm. The volumetric fractions calculation (figure 4b) demonstrates that the volumetric fraction of the base metal for the principal α-Mg phase is estimated at 85.4%, that of the eutectic phases at 13.8% and those of the precipitates at 0.8%. These results are in line with those in the literature and the diagram of the alloy phase AZ91 [18]. The large reduction of grains in the welded zone is confirmed by statistical distribution of the grains (Figure 5a) where the principal mode is 16µm.

a   b
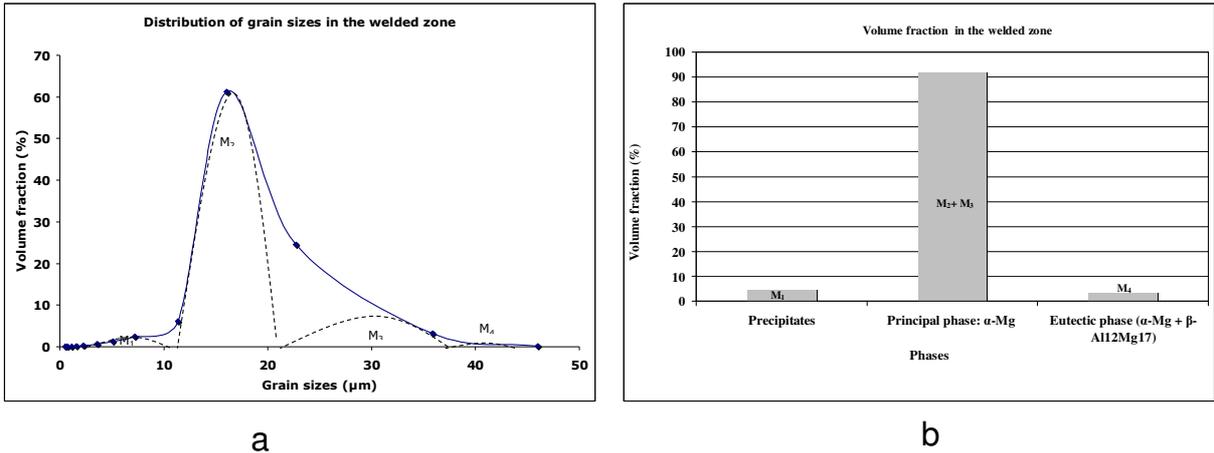
Figure 5: (a) Statistical distribution of the grain sizes of AZ91 alloys in welded zone.

(b) Volume fraction of the α-Mg grains and of the β-$Mg_{17}Al_{12}$ precipitates in the welded zone.

The volumetric fraction of the principal phase represented by modes 2 and 3 constitutes 96% of the matrix (Figure 5b). These results are still in line with those in the literature. The eutectic phase has almost disappeared in the welded zone.

4.4   Texture characterisation

By examining the intensity values, the texture of the base metal (BM) can be characterised by concentrated and strong reflections. These results can be viewed as a consequence of the grain size (50-200 µm) rather than texture. The irradiated volume is not representative of all sheets. On the contrary, the grain size in CWZ is fine (10 – 25 µm) so that the irradiated volume is statistically representative of the grain distribution. The texture analysis shows clearly that there is no texture. Indeed, ODF calculation indicates that more than 99% of the grains are randomly oriented. Likewise, there is no more texture in the HAZ with 90% of the grains being randomly oriented [14].

However, close to the surface, the AZ91 alloy exhibits two preferential orientations concerning 77% of the grains. The $\{10\bar{1}1\}$ pole figure shows that a large fraction of grains are oriented with pyramidal $\{10\bar{1}1\}$ planes parallel to the surface of the sheet. The intensity of the center of this pole figure is a tenfold improvement in intensity compared with other peaks. A close look at the position reveals that the normal axis is tilted at an angle of $\pm 4°$ from the normal sheet direction to the transverse direction and around the welding direction. The ODF calculation allows us to say that 71% of the grains have an orientation $\{10\bar{1}1\}\langle 34\bar{1}3\rangle$ corresponding to the 3 Euler angles ($\varphi_1 = 65{,}6°$, $\phi = 60{,}8°$, $\varphi_2 = 54{,}4°$). Likewise, the $\{10\bar{1}0\}$ pole figure shows the presence of a smaller proportion of grains with $\{10\bar{1}0\}$ planes parallel to the surface. Such grains show two other poles $P_i^{\{10\bar{1}0\}}$ and $P_j^{\{10\bar{1}0\}}$, on both sides of the centre, due to the multiplicity of the hexagonal symmetry, which is equal to three. These poles are tilted at 60° around the centre. The ODF calculation allows us to say that 6% about of the grains have an orientation $\{10\bar{1}0\}\langle 0\bar{3}34\rangle$ corresponding to the 3 Euler angles ($\varphi_1 = 65°$, $\phi = 90°$, $\varphi_2 = 60°$). Between the surface and the 200 µm depth, the texture decreases to disappear completely from 200 µm (Figure 6).
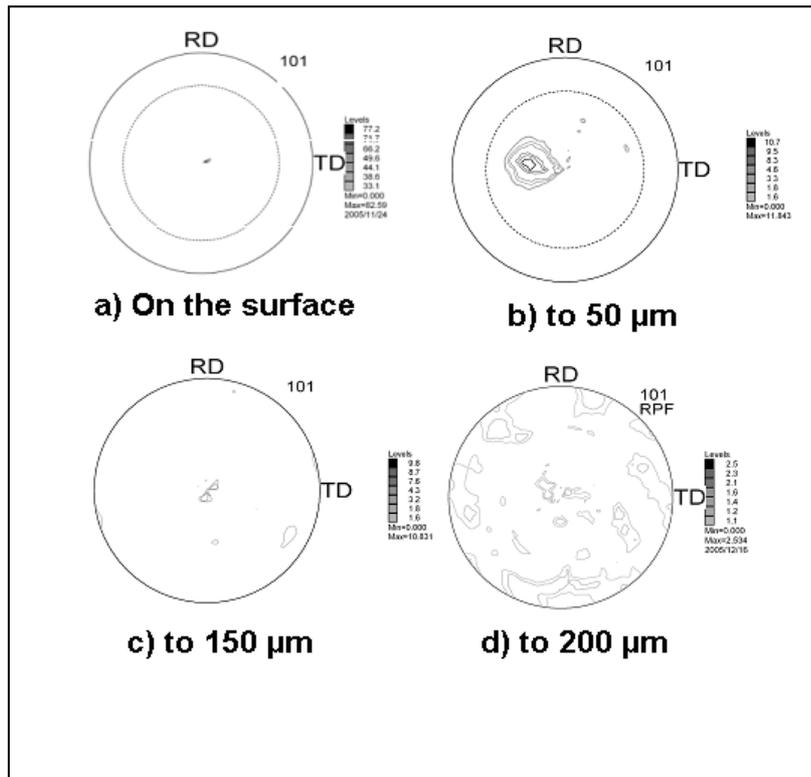
Figure 6: Evolution of the crystallographic texture (pole figure 101) from the surface to a depth of 200 µm: a) Texture to the surface, b) Texture to 50 µm, c) Texture to 150 µm, d) Texture to 200 µm

5. Experimental results of the mechanical properties

5.1 Microhardness characterization

Figure 7 shows the microhardness results, measured close to the surface on both sides of the linear weld in a profile including the base metal passing through the heat affected zone and the welded zone.
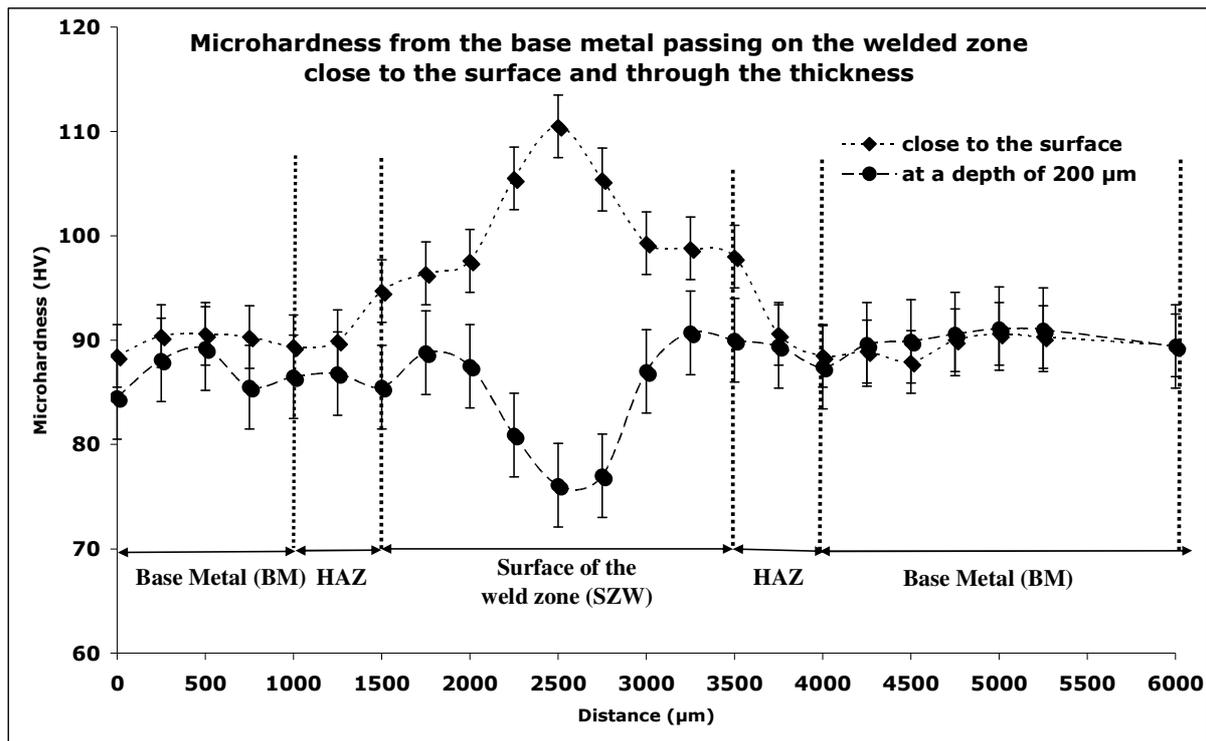
Figure 7: Microhardness from the base metal passing on the heat affected zone and the welded zone close to the surface and in the thickness at a depth about 200 μm.

The same measurement has been realized along the same profile and at a depth around 200 μm. Close to the surface, the microhardness varies from around 90 HV in the base metal and in the heat affected zone to 110 HV in the welded zone. Of the same form, through the thickness at a depth around 200 μm, the results show a different evolution than the surface concerning the BM and the HAZ, the microhardness is lower. In the depth, the evolution of the microhardness shows no statistical variation of the microhardness between the base metal, the heat affected zone and the welded zone contrary to the surface (Figure 7). We can see that the microhardness between the base metal, the heat affected zone and the core of the welded zone at a depth around 200 μm stays stable with a value of about 85 HV.

5.2 Residual stresses results

5.2.1 Distribution of the residual stresses at the surface of the assembled sheets

The measurements were undertaken in the welded zone, perpendicular to the weld line towards the base metal. Figure 8 shows the obtained results.
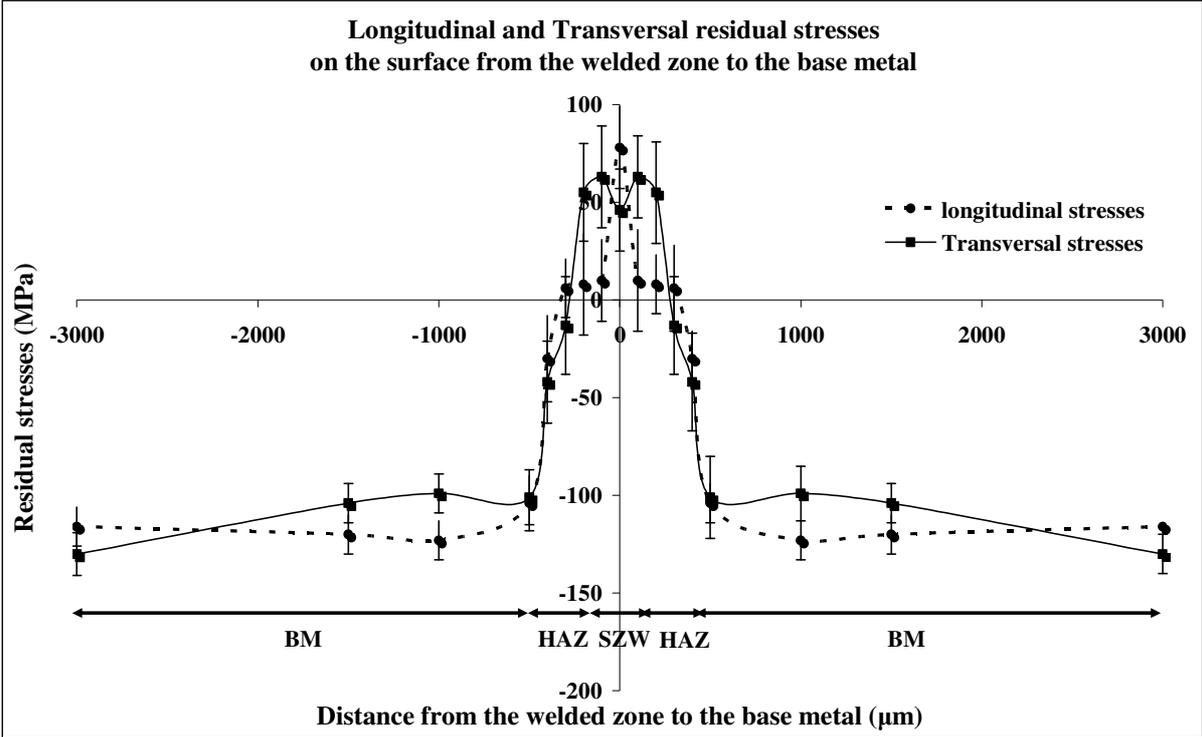
Figure 8: Longitudinal and transverse residual stresses close to the surface from the base metal until the welded zone.

The residual stresses far from the weld line are the same as those for the sheets before welding. The residual stresses are in compression, of the same value (~120 MPa) in all the directions of the plane. Opposite to this, the surface of the weld line is in traction, which can go up to about 80 MPa for the longitudinal component and about 46 MPa for the transverse component. In the heat affected zone, the values of the longitudinal and transverse residual stresses were respectively lower and greater compared to the welded zone. The magnitude of

longitudinal and transverse residual stresses was respectively around 70 MPa and 2 MPa. The difference between longitudinal and transverse stresses components confers certain anisotropy to the weld line, including the HAZ.

5.2.2 Distribution of the residual stresses though the thickness of the welded zone

The profiles of the average stresses through the thickness are plotted in the figure 9 for the longitudinal and transversal residual stresses.
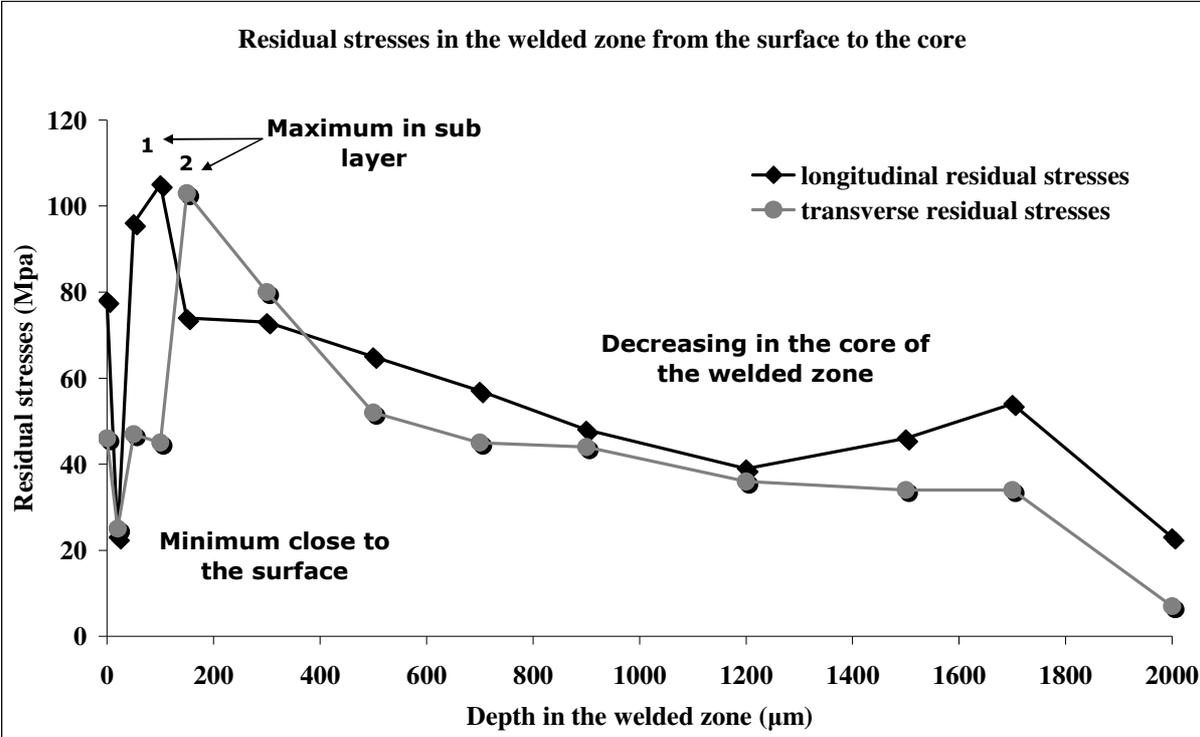
Figure 9: Longitudinal and transverse residual stresses from the welded zone close to the surface to the core of the welded zone.

With taken assumptions in this study, it is reasonable to consider them as representative of the average experimental stresses. These results are similar to those obtained by the other authors who have worked with the laser processing [18] and which evaluated the residual stresses by others methods [19]. We observed that the intensity of the longitudinal and transverse residual stresses components vary throughout the thickness of the weld line. It can be seen that the profile had a zigzag pattern, clearly asymmetrical. On the opposite face to the laser beam, the welding does not present a texture and is subjected to fairly weak traction residual stresses concerning the longitudinal and transversal component. On the other hand the face exposed to the laser beam presents a marked texture and tension residual stresses.

The maximum residual stresses are not on the surface but at a depth of 200 µm. At this depth the texture observed at the surface has disappeared.

6. Discussion

The results of this study demonstrate the microstructural and mechanical modifications induced by laser welding in a thin sheet of magnesium alloy (AZ91).

For the microstructural and anisotropic properties aspects we have based our work on the previously published public work [14] and references [3, 20, 21, 22, 23] which give a detailed description of microstructure and crystallographic texture modifications induced by laser welding.

We reiterate that the base metal is constituted of a number of different phases. The principal phase α-Mg, has an average grain size between 50 and 200 µm, and makes up 85% of the base metal. A eutectic phase (α-Mg + β-Mg$_{17}$Al$_{12}$), the average size of which is about 250µm, represents 13% of the base metal. Finally the observations have shown that there are β-

$Mg_{17}Al_{12}$ precipitates which are localised at the grain boundaries and some Al_3Mn_5 precipitates. The latter have an average size of between 2 and 10µm and represent 0.2% of the base metal. The base metal originally had a principally random distribution of grains [14].

In the thermally affected zone, the size of the grains remains unchanged whereas the eutectic phase (α-Mg + β-$Mg_{17}Al_{12}$) has disappeared to be replaced by α-Mg grains which have a higher aluminium content (8,51%). We can explain this final status by two successive stages. During the phase of increasing temperature, the added elements (Al and Mn) go into solution in the α-Mg phase. The cooling phase which follows is rapid and thermodynamic equilibrium is not reached which means that the added elements remain in supersaturated solid solution [29]. This zone is considered by many authors to be one of diffusion [25].

In the heart of the welded zone the observed microstructure is very small and constituted from β-$Al_{12}Mg_{17}$ precipitates which are localised in the boundaries between of the α-Mg phase grains which constitutes the matrix. The absence of eutectic phase again demonstrates that thermodynamic equilibrium is not reached. The kinematics of germination and growth of grains is essentially controlled by the power of the laser beam and the very high speed of cooling. The presence of two distinct phases has been attributed to the heterogeneous nature of the liquid in fusion and the cooling in non equilibrium [20, 21].

In a welded joint the superficial layer is distinguished by a loss in the level of aluminium (30%) and the presence of a strong crystallographic texture where 71% of the grains present a $\{10\bar{1}1\}\langle\bar{3}4\bar{1}3\rangle[1]$ type orientation [14]. The loss of aluminium has been attributed to exchanges with the gaseous phase [22]. The nature of the texture has been explained by the thermodynamic conditions of minimisation of surface energies [14, 23, 24] which results in the presence of columnar grain growth at the surface of the welded zone [25]. This textured zone disappears at a depth of about 200µm. Between the surface and the 200 µm depth, the

texture decreases to disappear completely from 200 µm. This change underlines the presence of a transition from columnar growth to equiaxial grain growth [24, 25].

From the mechanical properties standpoint, the study of microhardness and the evaluation of residual stresses demonstrate that laser welding induces particular profiles in the zones studied.

The results have enabled us to demonstrate that for microhardness that there are particular distributions in the different zones studied.

At the surface the results showed two zones (the HAZ and the SWZ) where the microhardness does not seem to conform only to the Hall and Petch effect [30] which states that micro hardness increases as grain size decreases. The microhardness in the HAZ (zone 4) is higher than in the base metal, even though the size of the grains is identical. This augmentation of microhardness has in part been explained by the contribution of added elements and particularly the increase in the level of aluminium in this zone (10%). These results were highlighted by the Shaw and Jones equation:

$$H = H_0 + K_1(X_{Zn} + 1/2X_{Al}) \qquad\qquad\qquad \text{Eq. 6}$$

for cases of rapidly solidified magnesium alloys [26]. Other studies have also demonstrated the presence of precipitates which are formed in this zone considered to be a zone of diffusion which contributes towards augmenting the microhardness [26].

Studying down through the depth of the metal shows that the superficial layer of the weld line presents a much increased hardness (110 HV) compared to the heart of the weld and the base metal.

The increase in microhardness compared to the base metal can be explained by the Hall and Petch relationship. But if we compare the SWZ to the center of the welded zone, we observe a variation in microhardness with no variation in size. Similarly the relationship proposed by Shaw and Jones is no longer verified [26]. The reduction in the amount of aluminium in this layer should lead towards a reduction in the micro hardness. Studies have demonstrated that microhardness can be increased by the presence of twinning and orientation of grains [27]. In this case two competing effects relating to the constraint- deformation response induced by the micro hardness test are put into effect: The work hardening at the surface which is due to the Hall and Petch effect (dislocations) and the Basinski mechanism [27] (reoriented regions and twinning). These regions being harder than the base matrix present higher microhardness values. In our study we did not find any evidence of twinning, but of a marked texture. The high increase in the microhardness of the surface of the welded zone compared to the centre of the welded zone was attributed in part to the influence of the texture, by recalling that the hardness test induces a plastic deformation which follows the normal direction of the surface. However the textured material is anisotropic compared to the plasticity [28]. In the present case, the $\{10\bar{1}1\}\langle\overline{34}\bar{1}3\rangle$ orientation of the grains following the pyramidal plane is not favorable to plastic deformation [29].

The origin of residual stresses and their evolution within a welded joint is difficult to evaluate because they are the result of a number of competing mechanisms: shrinkage changes in phase and microstructure [30]. In our case, the magnesium does not undergo a phase transformation, as is the case for aluminium alloys. Numerous studies have shown that when this is the case residual stresses are primarily a consequence of an inhibited shrinkage in the weld line and of the modified microstructure which is linked to strong temperature gradients, and to their distribution within the material [31, 32, 33].

At the surface, the results demonstrate that the base metal presents a state of compression, whereas the weld line is submitted to residual traction stresses. This state of compression has been attributed to the nature of the cooling, linked to the molding process. Cooling occurs by the diffusion of heat through the outer surfaces of the plates which are in contact with the mould walls. Furthermore the machining by milling of the surface of the base metal before welding accentuates the state of compression and explains the raised values (- 120 MPa) observed at the surface of the base metal. However, in the weld line the heat is evacuated by the plates and not the free surfaces. This leads to traction stresses. This evolution is in line with mechanical equilibrium. The welded zone exhibits residual traction stresses which are counter balanced by compression stresses in the base metal [34].

Furthermore, study of the state of surface stresses demonstrates some anisotropy: the residual stresses are not equibiaxial. We observe that the longitudinal component decreases from the center of the weld zone towards the base metal, whereas the transverse component remains high before a sudden reduction. These changes occur in the thermally affected zone, and are associated with numerous factors and by many authors with a zone of relaxation. The evolution of the longitudinal stress can be connected with the heat flow resulting from the mobile heat source that follows the welding direction. We can see two explanations of these evolutions. On the one hand, the effect of temperature and cooling speed gradients arise from the anisotropic heat flow [35], on the other, the anisotropy can be the result of a shrinking structure [36, 37]. The negligible thermal dilation of both plates prevents the free shrinkage of the weld line along the direction of the weld line. The same applies to the transverse component. The restricted shrinkage in the transverse plane arises from the clamping of the plates during welding. Even if the influence of the clamping is hard to evaluate experimentally, digital studies have shown that the field of residual stresses is strongly influenced by the geometry of the assembly [37, 38].

The study through the thickness of the welded zone shows that in general the profiles of the stresses reproduce the asymmetry of the welding process [38]. Their behaviour in tension and their variation have in part been explained by the influence of the thermal cycle on the origin of residual stresses and their evolution within the material [38, 39]. The residual stresses on the face exposed to the laser beam are elevated (up to 80 MPa) whereas the opposite face creates stresses of only 23 and 7 MPa respectively for the longitudinal and transverse stresses. This effect can also be explained by the fact that using inert gas ensures very rapid cooling of the superior face whereas the inferior face cools more slowly [40].

Finally we have noticed that over the first 200 micrometers the residual stresses present a particular evolution. The intensity of the stresses is not maximum at the surface of the welded zone (78 and 45 MPa respectively for the longitudinal and transverse constraints) as expected, but at a depth of 200µm the stress is 100 MPa. The presence of this maximum stress demonstrates that there is a stress gradient between the textured layer and the heart of the isotropic welded zone. This specific evolution has partly been explained by the plastic deformation of the superficial layer. By presenting a strong texture and an important loss of aluminum, the superficial layer is more sensitive to plastic deformation in the plane compared to the heart of the weld line which is isotropic [41].

These results can be compared to a thin coat deposit because these thin coatings are textured and the maximum stresses are found at the interface [42, 43].

In our study there is a transition zone with a continual evolution in properties, in particular an evolution of the texture between the outer surface and the depth at about 200 µm. It appears that the development of this texture affects the distribution of stresses with a relaxation of the stresses at the surface and a maximum in the under layer [43]. We explain these modifications

by the fact that the level of plastic flow, related to local stresses, is dependent on grain orientation [28, 44, 45, 46].

7. Conclusions

The set of results demonstrates that laser welding induces the presence of several distinct zones which have distinct microstructural and mechanical properties.

The base metal is constituted of several phases such as the principal α-Mg phase, the eutectic phase (α-Mg, β-$Mg_{17}Al_{12}$) and the Al_3Mn_5 precipitates. The average grain size varies from 50 to 250µm. The thermally affected zone presents sizes of 300 to 400µm. This zone no longer presents a eutectic phase but only the principal α-Mg phase. The precipitates are localised mainly around grain boundaries in the matrix. The level of aluminum is greater than the base metal. The heart of the welded zone is characterised by a number of microstructural and mechanical modifications. The grain size strongly diminishes and reaches an average size of between 10 and 25µm. The eutectic phase disappears. The matrix is principally constituted of α-Mg phase with β-$Mg_{17}Al_{12}$ precipitates localised around the grain boundaries. The chemical composition is comparable to that of the base metal [14]. Concerning the mechanical properties, this zone presents a reduction in microhardness which contradicts the law of Hall and Petch. The residual stresses are also modified because this zone is characterised by tensile stresses.

The main result has been the demonstration of a superficial layer at the surface of the welded zone. This layer demonstrates similarities with the heart of the welded zone concerning the size of the grains and the nature of the phases. Nevertheless, this layer presents a peculiarity of a marked crystallographic texture, a high degree of loss of aluminium as well as an elevated micro hardness. These characteristics disappear after a depth of 200µm in the welded zone. These modifications have been explained by the nature of the solidification which occur

under nonequilibrium conditions resulting in a columnar – equiaxial transition [14]. This transition has also been demonstrated in the profile of residual tension stresses which are at a maximum at the interface between at the superficial layer and the rest of the welded zone. These results have been explained by the anisotropic properties of the textured layer in relation to the plasticity.

This study has demonstrated that in the case of a heterogeneous and multiphase material that complex evolutions occur in the microstructural and mechanical properties due to laser welding. These results are considered as a basis for future investigation to better understand the microstructural and mechanical properties. Of note, it would be of interest to better comprehend the evolution of mechanical properties in relation to their microstructure and in particular the crystallographic texture.

References

[1]: P. Juijerm, I. Altenberger, B. Scholtes, Mater. Sci. Eng., 2006, vol. 426A, pp. 4-10.

[2]: T.L Teng, C.C. Lin, Inter. J. of Pressure Vessels and Piping, 1998, vol. 75, pp. 857-864.

[3]: D. Dubé, M. Fiset, A. Couture, I. Nakatsugawa, Mater. Sci. Eng., 2001, vol. 299A, pp. 38-45.

[4]: D.H. StJohn, A.K. Dahle, T. Abbott, M.D. Nave, Ma Qian, Miner. Metall. Mater. Soc., 2003, pp. 95-100.

[5]: S.H Wu, J.C. Huang, Y.N Wang, Metall. Mater. Trans., 2004, vol. 35A, pp. 2455- 2469.

[6]: C. Long, S. Ying, B. Shen, S. Qiu, X. ling, Y. Wang, Q. Peng, , J. of Nuclear Mater., 2003, vol. 321, pp. 60-69.

[7]: F. Caleyo, T. Baudin, M.H Mathon, R. Penelle, Eur. Phys. J. AP, 2001, vol. 15, pp. 85-96.

[8]: H.R. Wenk, K. Pawlik, J. Pospiech, J.S Kallend, Textures and Microstructures, 1994, vol. 22, pp. 233-260.

[9]: K. Pawlik, J. Pospiech, K. Lücke K., Proc. of ICOTOM-8, 1987, Santa Fe, USA, pp.531.

[10]: J. Jura, Scientific Bulletins of University of Mining and Metallurgy, 1993, n° 1530, Krakow, Poland.

[11]: T. R. Long, C. S. Smith, Acta Metall., 1957, vol. 5, pp. 200-207.

[12]: J.M. Sprauel, M. François, M. Barral, G. Beck, Elsevier Applied Sci., 1989, pp. 172-177.

[13]: M. François, J.M. Sprauel, J.L. Lebrun, Proc. 9th Int. Conf. on Experimental Mechanics, 1990, p. 1272-1280.

[14]: A. Kouadri, L. Barrallier, Mater. Sci. Eng., 2006, vol. 429A, pp. 11- 17.

[15]: F.J Humphreys, M. Hatherly, Editions Elsevier, 2004, pp. 555-556

[16]: J.M Fridy, K. Marthinsen, T.N Rouns, K.B. Lippert, E. Nes, O. Richmond, Proc. 3rd Int. Conf. on Aluminium, Trondheim, 1992, pp. 333.

[17]: A. Luo, Canadian Metall. Quarterly, 1996, vol. 35, pp. 375-383.

[18]: AB. Rhima, J. Bessrour, M. Bouhafs, R. Khadrani, Inter. J. of Thermal Sciences, 2003, vol. 42, pp. 759-776.

[19]: M. Härting, Act. Metall., 1998, vol. 46, pp. 1427-1436.

[20]: B.L. Mordike, T. Ebert, Mater. Sci. Eng., 2001, vol. 302A, pp. 37-45.

[21]: M. Maryan, G.R Edwards, Welding J., 2000, vol. 44, pp. 31-37.

[22]: Peng Liu, Yajiang Li, Haoran Geng, Juan Wang, Haijun Ma, Guolin Guo, Metall. Mater. Trans., 2006, vol. 37B, pp. 649-653.

[23]: A.N. Kalinyuk, N.P Trigub, V.N. Zamkov, O.M. Ivasishin, P.E. markovsky, R.V. Teliovich, S.L. Semiatin, Mater. Sci. Eng., 2003, vol. 346A, pp. 178-188.

[24]: Z.A. Matysina, Mater. Chem. and Phy., 1999, vol. 60, pp. 70-78.

[25]: W. Kurtz, C. Bezençon, M. Gäumann, Sci. Techn. of Advanced Mater., 2001, vol. 2, pp. 185-191.

[26]: C. Shaw, H. Jones, Mater. Sci. Eng., 1997, vol. 226-228A, pp. 856-860.

[27]: A.A. Salem, S.R. Kalidindi, R.D. Doherty, S.L. Semiatin, Metall. Mater. Trans., vol. 2006, 37A, pp. 259-268.

[28]: R. Gehrmann, M.M. Frommert, G. Gottstein, Mater. Sci. Eng., 2005, vol. 395A, 2005, pp. 338-349.

[29]: J.J Fundenberger, M.J Philippe, F. Wagner, C. Esling, Act. Metall., 1997, vol. 45A, pp. 4041-4055.

[30]: K. Dai, L. Shaw, Metall. Mater. Trans., 2003, vol. 37A, pp. 1133-1145.

[31]: W.G. Mao, Y.C. Zhou, L. Yang, X.H. Yu, Mech. of Mater., 2006, vol.38, pp. 1118-1127.

[32]: J.R. Cho, K.T. Conlon, R.C. Reed, Metall. Mater. Trans, 2003, vol. 37A, pp. 2935-2946.

[33]: L. Wagner, Mater. Sci. Eng., 1999, vol. 263A, pp. 210-216.

[34]: J.T. Al-Haidary, A.A. Wahab, E.H. Abdul Salam, Metall. Mater. Trans, 2006, vol. 37A, pp. 3205-3214.

[35]: J. Grum, R. Sturm, J. of Mater. Techn., 2004, vol. 147, pp. 351-358.

[36]: N.H. Pryds and X. Huang, Metall. Mater. Trans, 2000, vol. 33A, pp. 3155-3166.

[37]: T.L Teng, Chin-Ping Fung, Peng-Hsiang Chang, Intern. J. of Pressure Vessels and Piping, 2002, vol. 79, pp. 467-482.

[38]: M.V.R. S. Jensen, D. Dye, K. E. James, A. M. Korsunsky, S. M. Roberts, R. C. Reed, Metall. Mater. Trans, 2002, vol. 37A, pp. 2921-2931.

[39]: K. Dai, L. Shaw, Metall. Mater. Trans, 2003, vol. 37A, pp. 1133-1145.

[40]: W. Dong, H. Kokawa, S. Tsukamoto, Y. S. Sato, M. Ogawa, Metall. Mater. Trans, 2004,

vol. B, pp. 331-338.

[41]: I.C. Hsiao, S.W. Su, J.C. Huang, Metall. Mater. Trans, 2000, vol. 33A, pp. 2169-2180.

[42]: J. Pina, A. Dias, M. François, J.L Lebrun, Surf. Coat. Tech., 1997, pp.148-162.

[43]: C. Cevat Sarioglu, Surf. Coat. Tech., 2006, vol. 201, pp.707-717.

[44]: S.F. Su, J.C. Huang, H.K. Lin, N.J. Ho, Metall. Mater. Trans , 2002, vol. 33A, pp. 1461-1473.

[45]: S.R. Agnew, Ö. Duygulu, Inter. J. of Plasticity, 2005, vol. 21, pp. 1161-1193.

[46]: X. Wu, S. R. Kalidindi, C. Necker and A.A. Salem, Act. Mater., 2007, vol.55, pp. 423-432.